Materials Today Physics 64 (2026) 102107

Contents lists available at ScienceDirect

Materials Today Physics

journal homepage: www.journals.elsevier.com/materials-today-physics

Direct evidence of mixed-phase induced anomalous thermal transport in hybrid perovskite single crystals

Yuting Yu [a], Gan Zhang [b], Zifeng He [a], Jing Tu [a], Ankit Jain [c], Jonathan A. Malen [d], Derya Baran [e], Yee Sin Ang [f], Shusheng Xiong [g,h,i], Dawei Di [b,*], Wee-Liat Ong [a,j,**]

[a] ZJU-UIUC Institute, College of Energy Engineering, Zhejiang University, Haining, Jiaxing, Zhejiang, 314400, China
[b] State Key Laboratory of Extreme Photonics and Instrumentation, College of Optical Science and Engineering, ZJU-UIUC Institute, International Research Center for Advanced Photonics, Zhejiang University, Zhejiang, China
[c] Mechanical Engineering Department, IIT Bombay, Mumbai, 400076, India
[d] Department of Mechanical Engineering, Carnegie Mellon University, Pittsburgh, Pennsylvania, 15213, USA
[e] Material Science and Engineering Program, Physical Sciences and Engineering Division, King Abdullah University of Science and Technology, Thuwal, 23955-6900, Saudi Arabia
[f] Science, Mathematics and Technology, Singapore University of Technology and Design, 487372, Singapore
[g] Longquan Industrial Innovation Research Institute, Longquan, 323700, China
[h] College of Energy Engineering, Zhejiang University, Hangzhou, Zhejiang, 310027, China
[i] Provincial Key Laboratory of New Energy Vehicles Thermal Management, Longquan, 323700, China
[j] State Key Laboratory of Clean Energy Utilization, Zhejiang University, Hangzhou, Zhejiang, 310027, China

ARTICLE INFO

Keywords:
FDTR
Mixed phase
Hybrid
Thermal transport
Laser-based

ABSTRACT

The thermal conductivity of crystalline semiconductors is critical for their optoelectronic performance and is commonly described by the classical phonon gas model. Here, we report a clear violation of this conventional behavior during the phase transition of methylammonium lead bromide ($MAPbBr_3$) perovskite single crystals. Through transient frequency domain thermoreflectance experiments, an anomalous kink in thermal conductivity between 170 and 220 K is observed, disrupting the usual monotonic decrease with increasing temperature above the Debye temperature. Temperature-dependent X-ray diffraction (TDXRD) experiments reveal that a mixed orthorhombic-tetragonal phase exists in $MAPbBr_3$ from 140 K to 210 K. By combining TDXRD with phonon Wigner transport equation calculations, the origin of this anomalous thermal conductivity kink is attributed to two causes: the differences in the phonon properties between the tetragonal and orthorhombic phases and an increasing proportion of the tetragonal phase at increasing temperature. The notable differences in the phonon properties between these two phases, coupled with the potential differences in the properties of the charge carriers, can dramatically impact the optoelectronic performance of hybrid perovskites. Importantly, a similar kink is also observed within methylammonium lead chloride, suggesting such mixed-phase-induced thermal transport properties may be applicable to a broader class of perovskite semiconductors.

1. Introduction

The development of functional materials critically relies on reliable control and understanding of their thermal transport behaviors. Materials with high thermal conductivity are essential for efficient heat dissipation in electronic packaging and high-power devices, while those with low thermal conductivity are explored for thermoelectrics and thermal barrier coatings [1]. In simple crystalline solids, the lattice thermal conductivity (κ) follows a predictable temperature dependence: κ first increases with temperature (T) from 0 K due to increased heat capacity, peaks at intermediate T due to extrinsic scattering by boundaries or impurities, before decreases approximately as $1/T$ when intrinsic Umklapp scattering starts to dominate [2]. However, this conventional phonon gas model has failed to capture the unique transport properties in complex crystalline materials and thermal transport characteristics during phase transitions. Although recent developments

* Corresponding author.
** Corresponding author. ZJU-UIUC Institute, College of Energy Engineering, Zhejiang University, Haining, Jiaxing, Zhejiang, 314400, China.
E-mail addresses: daweidi@zju.edu.cn (D. Di), weeong@intl.zju.edu.cn (W.-L. Ong).

https://doi.org/10.1016/j.mtphys.2026.102107
Received 9 February 2026; Received in revised form 6 April 2026; Accepted 20 April 2026
Available online 21 April 2026

in the two-channel thermal transport models[3–5] have alleviated the understanding for complex crystals, phase transition induced transport characteristics are still unchartered. For example, the perovskite $RMnO_3$ family exhibits a diverse but unexplained temperature-dependent thermal transport behaviors arising from the Jahn-Teller distortion-induced competition between different magnetic orbitals [6]. Current thermal transport models also cannot adequately describe the nearly temperature-independent κ in non-spin ordered $TbMnO_3$/$DyMnO_3$ or the abrupt variations of κ during spin-order transitions in $RMnO_3$ (R= La, Eu, Gd, Y, Lu) [6]. These important but unexplained phenomena motivate further exploration of complex crystalline materials during phase transitions.

Hybrid pervoskites like methylammonium lead halide (i.e., $MAPbX_3$, X = I, Br, Cl) possess a unique organic-inorganic hybrid structure which also undergo temperature-driven molecular orientation-induced lattice distortions accompanied by phase transitions [7], providing an ideal platform for such exploration. $MAPbX_3$ perovskites have emerged as the new generation of light-absorbing layer of solar cells and light-emitting diodes due to their attractive optoelectronic properties and cost effectiveness[8–10]. A thorough understanding of their temperature-dependent thermal transport properties is therefore essential for improving the device performance and operational stability. While many experimental studies have explored the thermal conductivity of $MAPbX_3$[11–19], most have concentrated on temperatures above 290 K [11–15]. The steady state method has been used to measure the temperature-dependent thermal conductivity of $MAPbI_3$ to temperatures as low as 7 K, showing a crystalline-like trend with higher thermal conductivity at lower temperatures [16,17]. It should be noted that such steady state measurement is complicated by its inherent radiative losses, which requires additional corrections for a complete assessment [17]. Comparing with $MAPbI_3$, the thermal conductivities of $MAPbBr_3$ and $MAPbCl_3$ at low temperatures have received limited experimental attention despite their excellent environmental stability [20]. Current theoretical studies have predicted a simple crystalline thermal conductivity behavior for $MAPbX_3$[21–26]. Recent studies have, however, challenged this simple picture[13,18,19,27–29]. Among which is an anomalous upward thermal conductivity trend measured during the phase transitions in $MAPbBr_3$ and $MAPbCl_3$ [18,19], which remains unexplored.

In this study, the frequency domain thermoreflectance (FDTR) method is utilized to measure the thermal conductivity trends of single crystal $MAPbBr_3$ in the temperature range of 100-350 K. Surprisigly, the thermal conductivity of $MAPbBr_3$ exhibits a clear anomalous kink near 210 K. To investigate the source of this kink, temperature-dependent X-ray diffraction (TDXRD) measurements is performed to study the structural characteristic of $MAPbBr_3$. Our investigations reveal the coexistence of tetragonal and orthorhombic phases between 140 K and 210 K. Analysis of the temperature-dependent FDTR and TDXRD data showed that this mixed-phase is present within the thermal penetration depth of FDTR measurement. Using the lattice dynamics-based phonon Wigner transport equation (LD-PWTE) method [3,30], this anomalous thermal conductivity kink is related to the difference in the thermal conductivity of each phase and the evolution of their relative quantity with temperature. Furthermore, the observation of a similar anomalous thermal conductivity kink in $MAPbCl_3$ between 170 K and 200 K suggests that the mixed-phase-induced thermal transport behavior may be observable in a broader range of hybrid perovskites with first-order phase transitions where phases with distinct thermal conductivities coexist. This research highlights a new low-temperature thermal transport phenomenon for the hybrid perovskite family, offering valuable experimental evidence and insights detected through careful analysis of the transient-based FDTR data. As charge carrier dynamics of the distinct phases exhibit marked differences due to their distinct electronic structures [31,32], the coexistence of the mixed-phase perovskites can significantly influence their optoelectronic performance, playing a vital role to improve hybrid perovskite solar cells operating at low temperatures.

2. Results and discussion

The structure of $MAPbX_3$ (X = I, Br, Cl) is temperature-dependent, with elevated MA molecular dynamic disorder but reduced octahedra distortion at increased temperatures [33,34]. As shown in Fig. 1(a), $MAPbX_3$ generally undergoes two sequential phase transitions with increasing temperature. The currently accepted first phase transition (Transition I) is from the orthorhombic to tetragonal, where higher temperatures weaken the constrained vibration of the MA molecules about their local equilibrium position [40]. This imparts certain rotational freedom to the MA molecules to explore a larger set of configurations in the tetragonal phase [31,40]. The second one (Transition II) is from the tetragonal to cubic phase. Here, the MA molecules reorientate quickly with anharmonic dynamics, resulting in a temporal-averaged cubic-like lattice with non-tilted octahedra [32,41]. Earlier experiments on $MAPbI_3$, $MAPbBr_3$, and $MAPbCl_3$, have found that the Transition I occurs at ~162 K, ~147 K, and ~172 K, while Transition II happens at ~330 K, ~232 K, and ~179 K, respectively [35–39].

The thermal conductivity of single crystal $MAPbBr_3$ was measured using the FDTR setup (Fig. 1(b)) between 100 K and 350 K (Details in the Methods). Results in Fig. 1(c) depict the measured thermal conductivity as a function of temperature. Our measured room-temperature thermal conductivity values are 0.41 ± 0.04 W m^{-1} K^{-1} for the single crystalline $MAPbBr_3$, agreeing with previous results [12,13]. The thermal conductivity trend generally decreases with increasing temperature, except around the phase transition regions. The thermal conductivity of $MAPbBr_3$ anomously increases upwards around the Transition I temperature at 147 K and kinks near 210 K. Similarly, our measurements on $MAPbCl_3$ within the same temperature range reveal a comparable kink near 200 K (Fig. S1 of the Supplementary Information). Except for this kink, our thermal conductivity trend is generally crystalline-like [18], which has been attributed to the localized vibrational states and dynamic disorder of the MA molecules [7,42,43]. However, the notable thermal conductivity kink in our experiments disagrees with the existing recorded trend over a sizeable temperature range. Furthermore, this kink falls outside the temperature range that can be affected by the latent heat [44,45], suggesting that a different mechanism is present.

To elucidate the origin of this kink, temperature-dependent X-ray diffraction (TDXRD) was performed on $MAPbBr_3$ to investigate the structural changes. The TDXRD patterns in Fig. 2(a) for temperatures ranging from 140 K to 220 K, have diffraction peaks at 14.70°, 21.21°, 30.12°, 33.78°, 37.15°, 43.18°, and 45.93°, which are consistent with previous studies [46,47]. We analyzed the three diffraction peaks with the highest intensity, which are at 14.70°, 30.12°, and 33.78°(Fig. 2(b)–(d)). The peak at 14.70° displays a steady shift towards smaller diffraction angles with decreasing temperatures (Fig. 2(b)). However, the magnitude of this shift becomes smaller below 200 K, which typically signifies a structural phase transition [46]. This phase transition is more obvious from the peaks around 30.12° and 33.78° (Fig. 2(c)–(d)). As the temperature cools below 220 K, the single diffraction peak (peak 1 in Fig. 2(c)–(d)) broadens and a second but smaller peak (peak 2 in Fig. 2(c)–(d)) grows at a lower diffraction angle (see Diffraction Peak Analysis in Supplementary Information for more details). The development of this bimodal diffraction pattern from 210 K to 140 K is consistent with previous research [47], which signifies a portion of the tetragonal $MAPbBr_3$ (t-$MAPbBr_3$) gradually converts to the orthorhombic phase (o-$MAPbBr_3$), creating a mixed o-$MAPbBr_3$ and t-$MAPbBr_3$ crystal.

Several prior studies have reported the coexistence of the orthorhombic and tetragonal phase in perovskites [48–52] over a range of temperatures, which can be influenced by various factors such as synthesis method and morphology of the sample [53,54]. While many earlier studies have reported such coexistence in thin films [55] over a wide range of temperatures (e.g, more than 40 K in $MAPbI_3$ films) [48,

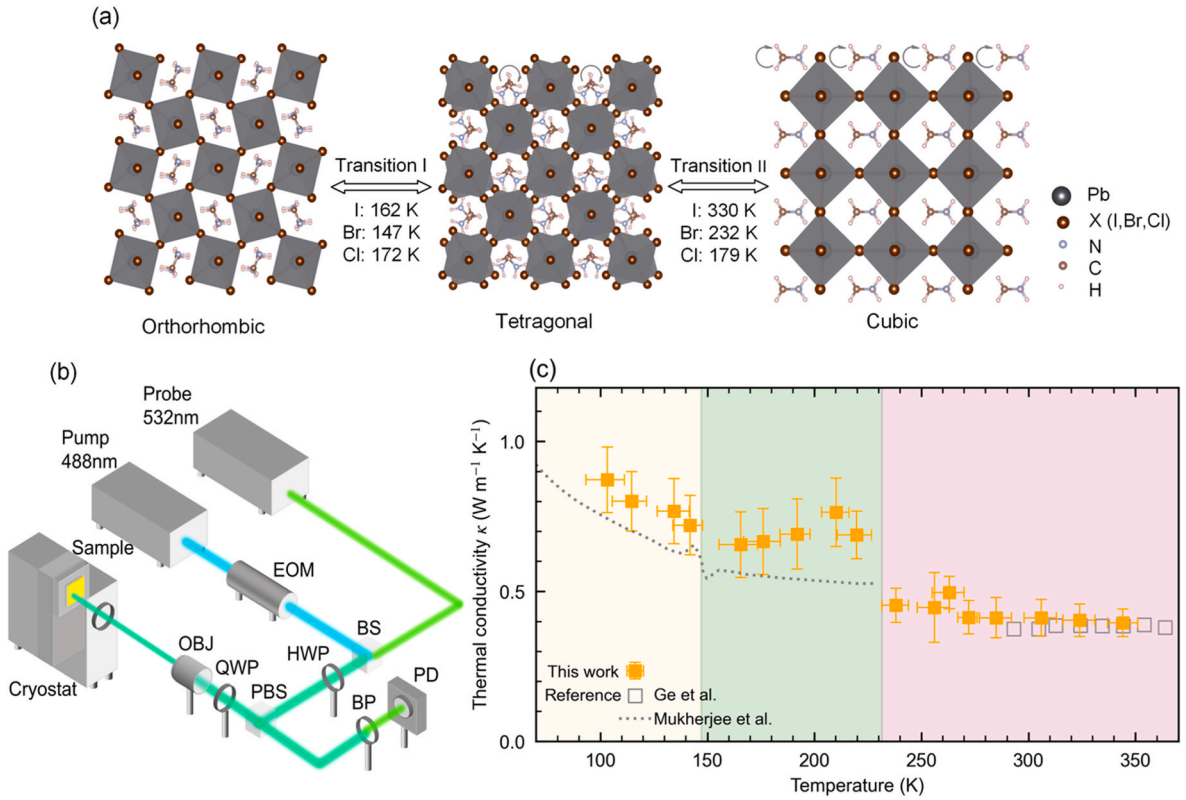

Fig. 1. (a) Common phase transition of $MAPbX_3$ (X = I, Br, Cl). **(b)** Schematic of the FDTR experimental setup. The abbreviations are EOM (electro-optic modulator), BS (beam splitter), HWP (half wave plane), PBS (polarized beam splitter), QWP (quarter wave plane), OBJ (objective length), BP(bandpass filter) and PD (photodiode detector). **(c)** The thermal conductivity of $MAPbBr_3$ single crystals measured in our FDTR experiment at temperatures from 100 to 350 K. The orange solid markers are from this work, and the dotted line (using steady state method) and hollow squares (using laser flash apparatus) are taken from Ref. [18] and Ref. [14], respectively. The three different background colors (light yellow, light green and light pink) correspond to the temperature ranges of three different phases (orthorhombic, tetragonal, and cubic respectively) of single crystal $MAPbBr_3$ from the literature[35–39]. Note that the measured thermal conductivity values are plotted against the corrected temperature after considering the average steady-state temperature rise near sample surface, with horizontal error bars representing the temperature range probed within the maximum thermal penetration depth in the sample.

51,53], recent findings have confirmed similar coexistance in powdered and single crystalline form, over a temperature range spanning more than 40 K in $MAPbI_3$ [54] and 50 K in $MAPbBr_3$ [46,56]. Our TDXRD result is consistent with previous results, showing a mixed phase of o-$MAPbBr_3$ and t-$MAPbBr_3$ over a large temperature range from 140 K to 200 K (i.e., a span of 60 K), which is a characteristic of a first-order phase transition [44,57].

Phase transition can impact the measurement of thermal properties like thermal diffusivity [44,45]. The analysis of the TDXRD data provides a method to quantify structural variation during phase transition in the $MAPbBr_3$ for our temperature-dependent FDTR measurements. Accounting for the temperature rise produced by the lasers used in FDTR is, thus, critical for obtaining accurate results and trends, as this temperature rise may lead to a localized phase transition within the measured region [58]. Fig. 3 shows the steady-state temperature rise distribution in the single crystal $MAPbBr_3$ at selected cryostat temperatures (T_0) in our FDTR experiment, with the average corrected surface temperature (T_f) also indicated (see Temperature rise correction in the Supplementary Information for the correction procedures). As our XRD result indicates that a pure t-$MAPbBr_3$ only exists above 210 K (see Diffraction Peak Analysis in Supplementary Information), we used this temperature as a cutoff in Fig. 3 to assess the possible phases in $MAPbBr_3$ during an FDTR experiment. The frequency of the pump laser in our FDTR experiment is regulated by an electro-optical modulator in the range from 60 kHz to 6 MHz, and the thermal penetration depth (TPD) is the maximum (minimum) at 60 kHz (6 MHz). Within the maximum TPD, only a mixed phase of o-$MAPbBr_3$ and t-$MAPbBr_3$ exists in the probed region when T_f is below 207 K, as shown in Fig. 3(a)–(d). When T_f is raised above 207 K, a pure t-$MAPbBr_3$ region appears near the sample surface and increases in size with rising temperatures [Fig. 3(e)–(f)]. This result suggests that the thermal conductivity measured in our FDTR experiment is for a mixed phase of o-$MAPbBr_3$ and t-$MAPbBr_3$ when T_f is below 207 K. Detailed phase distribution maps in the sample during FDTR measurement under different temperatures are available in Fig. S7 (see Structural Evolution Induced by Steady-State Temperature Rise in FDTR in Supplementary Information). It is important to note that although the average steady-state temperature rise ($\Delta T = T_f - T_0$) of the sample surface is above 24 K at each T_f, the maximum temperature difference sensed by FDTR due to the maximum TPD in the sample is less than 18 K, as indicated by the horizaontal bar at each datapoint in Fig. 1 (c).

Using the whole-pattern fitting (WPF) refinement analysis on the TDXRD data, the structure of the two coexistent $MAPbBr_3$ phases are determined to be $Pna2_1$ for o-$MAPbBr_3$ and $I4/mcm$ for t-$MAPbBr_3$ (see Whole-pattern fitting refinement analysis in Supplementary Information). Fig. 4(a) contains these crystal structures, and Table S2 contains the lattice parameters of each phase under different temperatures. The volume fraction (η) of each crystal structure at the different temperatures in Fig. 4(b) is obtained by calculating the relative ratio of the fitted intensity of corresponding peak near 30.12° and 33.78°(See Volume fraction analysis and Eqs. (S3)-(S4) in Supplementary Information) [59]. With increasing temperature, the proportion of tetragonal phase ($\eta_{t-MAPbBr_3}$) increases while the proportion of orthorhombic phase ($\eta_{o-MAPbBr_3}$) decreases, culminating to a pure t-$MAPbBr_3$ between the temperature of 210 K to 232 K.

Using the above relative fraction of the mixed phase, lattice

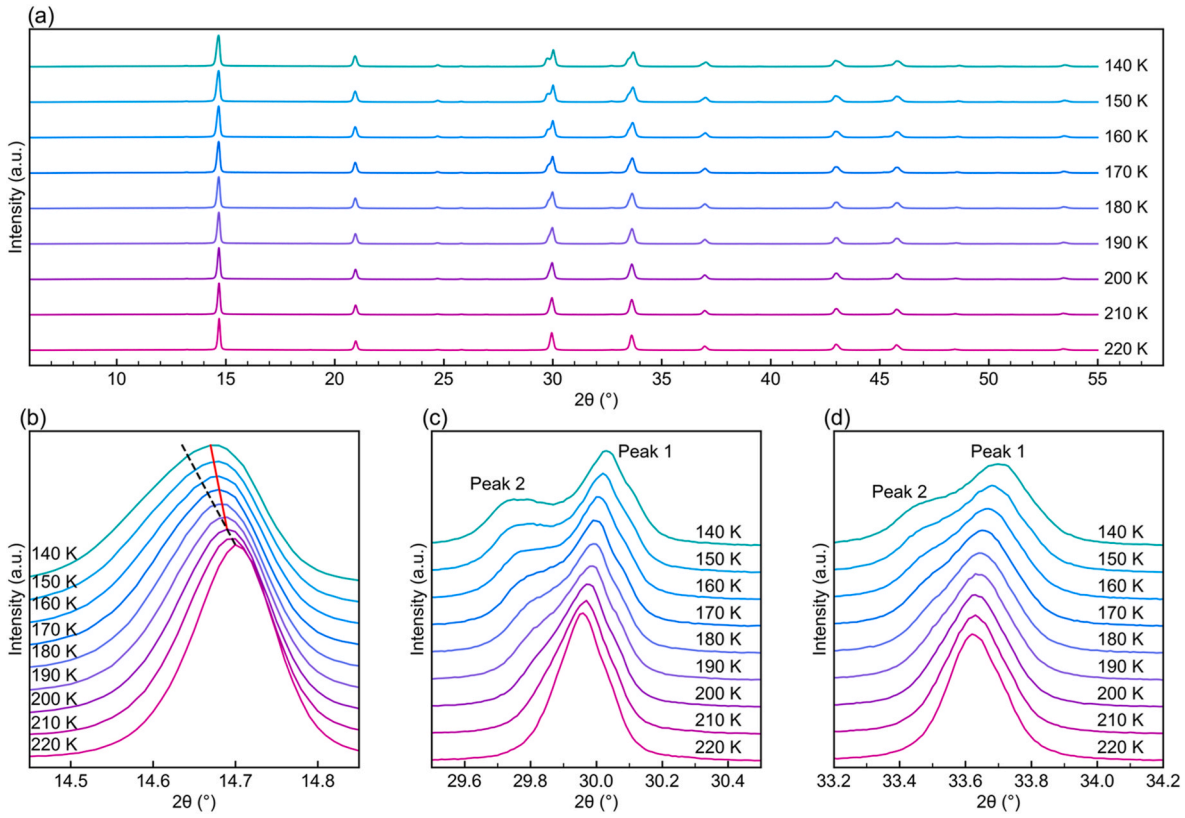

Fig. 2. (a) Powder TDXRD diffraction patterns of $MAPbBr_3$ at the temperatures of 140-220 K with diffraction angles (2θ) range from 6° to 55°. The diffraction pattern details around **(b)** 14.70°, **(c)** 30.12° and **(d)** 33.78°. The black dotted line in **(b)** represents the linear extrapolation using the diffraction peak positions above 200 K, while the red solid line connects the diffraction peak positions below 200 K.

dynamics-based phonon Wigner transport equation (LD-PWTE) method [3,30] which intrinsically incorporates quantum statistics was employed to calculate the thermal conductivity of $MAPbBr_3$ between 140 K and 350 K. The LD-PWTE method accounts for the dual contributions of phonons to thermal transport process: the population (κ_p) channel, arising from particle-like phonon propagation through the diagonal terms of the heat flux operators, and the coherence (κ_c) channel, which captures wave-like phonon propagation via the off-diagonal terms [30]. As pointed out in the literature, the coherence (κ_c) channel maybe significant in strongly anharmonic crystals, such as halide perovskites [3]. Using the LD-PWTE method, we calculated the thermal conductivities of pure o-$MAPbBr_3$ and t-$MAPbBr_3$ between 140 and 220 K (Fig. 4(b)). It is worth noting that, consistent with previous studies, the coherence channel makes a non-negligible contribution in both o-$MAPbBr_3$ and t-$MAPbBr_3$, as shown in Fig. S9. As a first approximation to estimate the thermal conductivity of the mixed phase $MAPbBr_3$ (κ_{mixed}) for temperatures below 210 K, we applied a simple mixing rule to the thermal conductivity and volume fraction (η) of the two phases,

$$\kappa_{mixed} = \eta_{o-MAPbBr_3}\kappa_{o-MAPbBr_3} + \eta_{t-MAPbBr_3}\kappa_{t-MAPbBr_3} \quad (1)$$

Given the strong anharmonicity of $MAPbBr_3$, coupled with the low thermal conductivity contrast between the coexisting o-$MAPbBr_3$ and t-$MAPbBr_3$ phases, it is physically reasonable to employ this first-order mixing rule as a reliable and computationally robust approximation for our system [60,61]. Results from Eq. (1) is plotted and compared to the FDTR results in Fig. 4(c). As shown in Fig. 4(c), κ_{mixed} agrees well with the FDTR experiment results with an average deviation of 5.3% over the entire mixed-phase temperature range from 140 K to 220 K, showing a similar kink which reach a maximum near 210 K. As demonstrated by our calculations in Fig. S9, thermal conductivities of both pure o-$MAPbBr_3$ and t-$MAPbBr_3$ decrease with increasing temperature across the entire mixed-phase range (also shown in Fig. 4(b)). This reduction can be mainly attributed to the significant deacrease in the population-channel (κ_p), given that the coherence-channel (κ_c) slightly increases with temeprature (Fig. S9(a)–(c)). The decrease in the population channel originates from enhanced phonon scattering rates at higher temperatures, while the phonon group velocities are largely unchanged (Fig. S9(f)). Moreover, although the mode-resolved phonon group velocities and lifetimes are comparable in the two phases (Fig. S9 (d)–(e)), the mode-averaged properties (Fig. S9(f)) reveal that both phonon group velocities and lifetimes are consistently higher in t-$MAPbBr_3$ than in o-$MAPbBr_3$ throughout the mixed-phase region. Consequently, t-$MAPbBr_3$ exhibits a higher thermal conductivity than o-$MAPbBr_3$, leading to the thermal conductivity maximum after all the mixed phase fully converts to a pure t-$MAPbBr_3$ phase above the temperature of 210 K. Our theoretical calculations confirm that the kink in thermal conductivity of $MAPbBr_3$ observed in the FDTR experiment is due to the existence of a mixed phase in the sample, with the o-$MAPbBr_3$ and t-$MAPbBr_3$ coexisting.

It is worth noting that since the mixed-phase-induced thermal conductivity kink was observed in both $MAPbCl_3$ and $MAPbBr_3$ in our study, we expect this anomaly to be a common feature of first-order transitions in other hybrid perovskites (e.g., $MAPbI_3$ and FA-based systems) where phases with distinct thermal conductivities coexist. Its occurrence and observability require a wide temperature window of the phase coexistence and a slow intrinsic phase transition rate. The width of this temperature window is generally influenced by various factors, such as the synthesis method and the morphology of the sample [53,54]. While the phase transition rate is inversely proportional to the energy barrier of phase transition process, which is further modulated by extrinsic factors like crystal domain size and residual stress [44,62,63].

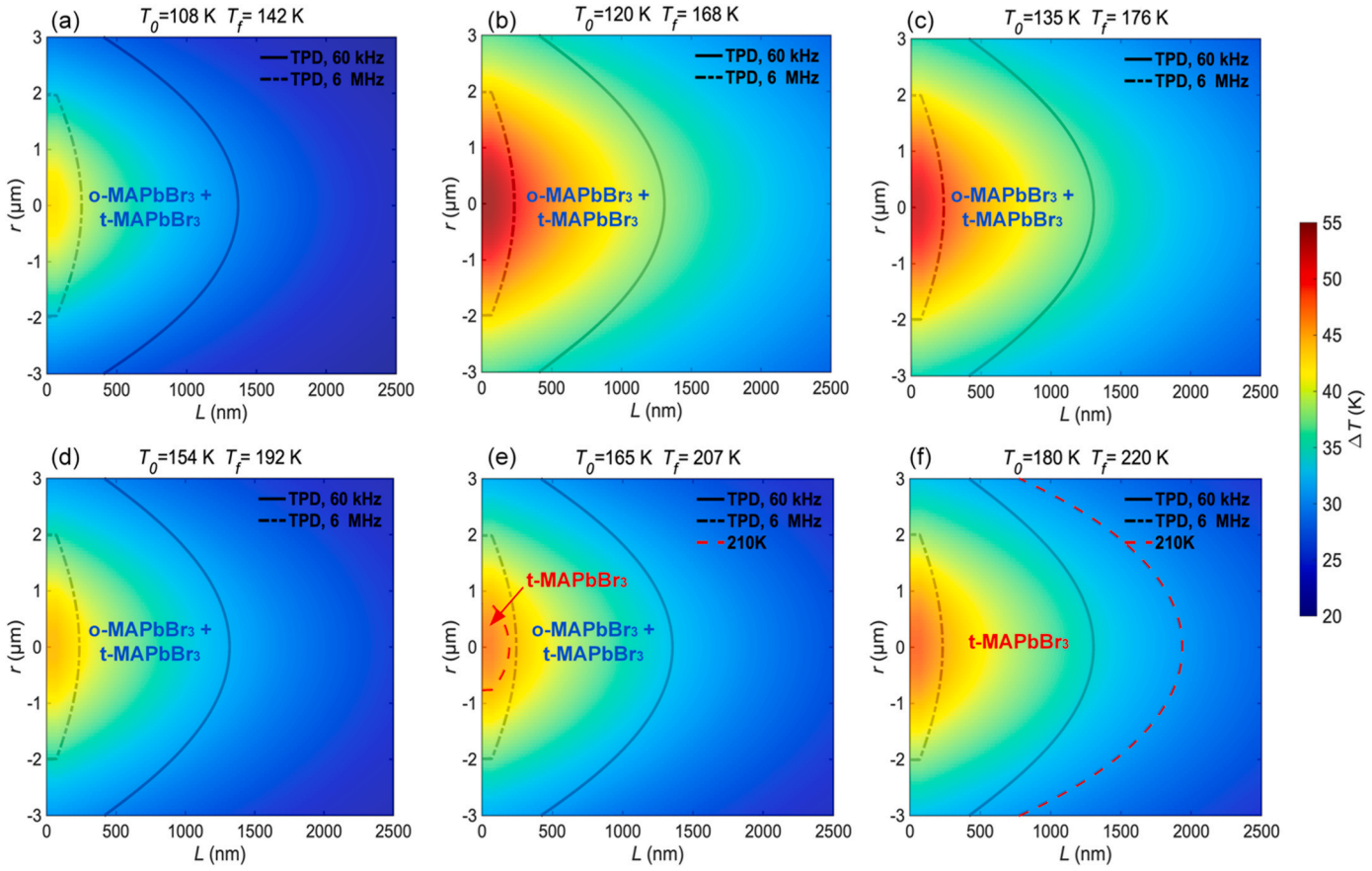

Fig. 3. Steady state temperature rise profiles for $MAPbBr_3$ single crystal induced by pump laser in FDTR experiment at different initial temperatures: **(a)** 108 K; **(b)** 120 K; **(c)** 135 K; **(d)** 154 K; **(e)** 165 K; **(f)** 180 K. L and r represent the depth and radius of the sampling point from the pump laser. T_0 is the initial temperature of sample controlled by the cryostat and ΔT is the steady-state temperature rise induced by the pump laser, T_f is the average corrected surface temperature after considering ΔT. The red dashed line indicates the 210 K isotherm which represents the boundary between the mixed o-$MAPbBr_3$ and t-$MAPbBr_3$ phase and the pure t-$MAPbBr_3$. The black solid (dashed) line is the maximum (minimum) thermal penetration depth (TPD) in the sample. The thermal penetration depth ranges from 100 nm to 1500 nm at $r = 0$, depending on the applied modulation frequency from 6 MHz (black dash line) to 60 kHz (black solid line).

3. Conclusion

In summary, the temperature-dependent thermal conductivity of single crystal $MAPbBr_3$ was measured with FDTR in the temperature range of 100 K-350 K. Different from a typical crystal where thermal conductivity decreases with increasing temperature, an unusual kink near 210 K was observed. The TDXRD experiment revealed coexistent o-$MAPbBr_3$ and t-$MAPbBr_3$ phases below the temperature of 210 K throughout the thermal penetration depth of the FDTR measurement. By performing LD-PWTE calculation, the contributions of each phase to the overall thermal conductivity of the mixed phase $MAPbBr_3$ were decoupled, suggesting that the gradual transition of the mixed phase $MAPbBr_3$ to a pure t-$MAPbBr_3$ over the temperature range is responsible for the kink. Our work directly links the structural phase transition to the measured anomalous thermal conductivity trend, thereby demonstrating that a mixed-phase state can lead to a unique thermal transport phenomenon. Moreover, the observation of a similar thermal conductivity kink in $MAPbCl_3$ near 200 K suggests that this mixed-phase-induced phenomenon may be common in a broader range of perovskite materials. These findings offer new insight into the thermal transport properties of halide perovskites, which are crucial for their optoelectronic applications.

4. Methods

4.1. Sample preparation

$MAPbBr_3$ and $MAPbCl_3$ single crystals were synthesized using the anti-solvent vapor-assisted crystallization (AVC) method following previous literature [64]. The methylammonium bromide (MABr, ≥99.5%), methylamine hydrochloride (MACl, ≥99.5%), lead bromide ($PbBr_2$, >99.99%), lead chloride ($PbCl_2$, >99.99%) were purchased from Xi'an Yuri Solar Co. Ltd (China). The N, N-dimethylformamide (DMF,≥99.9%), dimethyl sulphoxide (DMSO, anhydrous, ≥99.9%) and dichloromethane (DCM,≥99.5%) were sourced from Sigma Aldrich. All salts and solvents were used as received without any further purification. $PbBr_2$ and MABr ($PbCl_2$ and MACl) were dissolved in DMF (DMSO) at a 1:1 M ratio (1.0 M), and $MAPbBr_3$ ($MAPbCl_3$) single crystals were grown along with the slow diffusion of the vapor of the anti-solvent DCM into the solution.

4.2. Temperature-dependent X-ray diffraction (TDXRD)

Temperature-dependent powder XRD were performed to characterize the structure of $MAPbBr_3$ at the temperature range of 140-220 K. The temperature-dependent XRD measurement was conducted using a

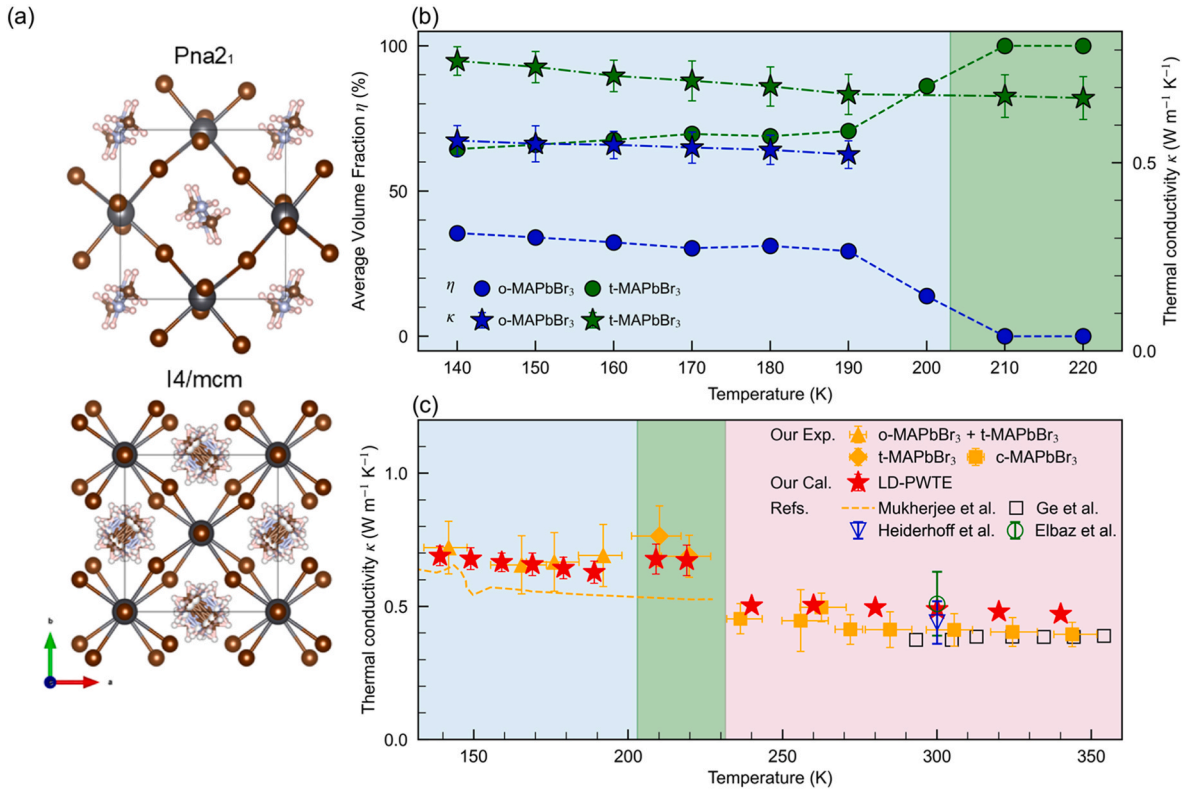

Fig. 4. (a) The crystal structures of o-$MAPbBr_3$ (top) and t-$MAPbBr_3$ (bottom). **(b)** The volume fraction η_i (left axis) and the thermal conductivity κ_i (right axis) of each phase i (i = o-$MAPbBr_3$, t-$MAPbBr_3$) under different temperatures. **(c)** The comparison of thermal conductivity for mixed phase $MAPbBr_3$ derived from theoretical LD-PWTE calculation and FDTR experiment. Our results show excellent agreement with the measurements reported by Mukherjee et al. using the steady-state method at low temperatures [18], and by Ge et al. employing the laser flash method at high temperatures [14]. Furthermore, our data closely match the room-temperature values obtained by Elbaz et al. via FDTR [12], as well as those measured by Heiderhoff et al. using the 3ω method [13]. The light blue region in (b) and (c) represent the mixed phase of o-$MAPbBr_3$ and t-$MAPbBr_3$, while the green region indicates the pure t-$MAPbBr_3$ phase within the corresponding temperature ranges. The pink region in (c) denotes a pure cubic phase in this temperature interval.

powder X-ray diffractometer (Rigaku Smart Lab 9 KW) with Cu-Kα radiation (λ = 1.54059 Å). The step size and scan rate for each measurement were 0.01° and 0.10° s^{-1}, respectively. A millimeter size bulk single crystal $MAPbBr_3$ sample was grinded into a fine powder for the XRD experiment. The cryogenic temperature was controlled by helium compressor at a ramp rate of 2 K min^{-1} and the sample fixed at each temperature for 30 min to stabilize before the XRD experiment.

4.3. Temperature dependent thermal conductivity measurement

To experimentally measure the low temperature thermal transport behavior of single crystal $MAPbBr_3$ and $MAPbCl_3$, we perfom frequency-domain thermoreflectance (FDTR) measurement [65] on the samples in a cryogenic chamber (Montana Cryostation S50), between the temperature of 100 K and 350 K at a rate of 2 K min^{-1}. At each targeted temperature, the sample is further equilibrated for 30 min before any FDTR measurement was conducted. In our FDTR setup, an intensity-modulated blue pump laser (488 nm) heats the sample surface sinusoidally, which was coated with 70 nm gold transducer to improve the optical reflectance signal. A green probe laser (532 nm) measures the resulting temperature response of the surface gold layer. The pump laser is modulated in the frequency range from 60 kHz to 6 MHz by an electro-optical modulator. The phase lag between the pump laser (heating) and probe laser (temperature) are measured by a lock-in amplifier as a function of modulation frequency. The thermal conductivity of samples were then extracted by fitting phase lag signals with a well-established multilayer heat conduction model [66,67]. The fitting parameters and sensitivity analysis [68,69] of our FDTR experiment were shown in the FDTR experiment details in the Supplementary Information.

4.4. Lattice dynamics based phonon wigner transport equation calculation (LD-PWTE)

The thermal conductivity was calculated by employing the lattice dynamics-based phonon Wigner transport equation (LD-PWTE) method [3,30]. This method can consider the particle-like and wave-like phonon thermal transport which corresponds to population-channel and coherence-channel thermal conductivity respectively. The population-channel thermal conductivity along α direction (κ_p^α) under the single-mode relaxation time approximation [3] can be expressed as:

$$\kappa_p^\alpha = \frac{1}{V}\frac{\hbar^2}{k_B T^2}\sum_{q,s}\omega^2(\boldsymbol{q})_s n(\boldsymbol{q})_s(n(\boldsymbol{q})_s+1)\nu^\alpha(\boldsymbol{q})_{s,s}\nu^\alpha(\boldsymbol{q})_{s,s}[\Gamma(\boldsymbol{q})_s]^{-1} \quad (2)$$

where V,T, k_B is the volume, temperature of the system and the Boltzmann constant respectively. $\nu^\alpha(\boldsymbol{q})_{s,s}$ is the group velocity of the phonon mode s of wavevector $\boldsymbol{q}$ along the α direction, and $\Gamma(\boldsymbol{q})_s$ is the linewidth

of the phonon mode s.

The coherence-channel thermal conductivity along α direction (κ_c^α) is given by [3]

$$\kappa_c^\alpha = \frac{1}{V}\frac{\hbar^2}{k_B T^2}\sum_{\boldsymbol{q}}\sum_{s\neq s'}\frac{\omega(\boldsymbol{q})_s+\omega(\boldsymbol{q})_{s'}}{2}\cdot\frac{\omega(q)_s n(\boldsymbol{q})_s(n(\boldsymbol{q})_s+1)+\omega(\boldsymbol{q})_s n(\boldsymbol{q})_{s'}(n(\boldsymbol{q})_{s'}+1)}{4(\omega(\boldsymbol{q})_s-\omega(\boldsymbol{q})_{s'})^2+(\Gamma(\boldsymbol{q})_s+\Gamma(\boldsymbol{q})_{s'})^2}\times\nu^\alpha(\boldsymbol{q})_{s,s'}\nu^\alpha(\boldsymbol{q})_{s,s'}(\Gamma(\boldsymbol{q})_s+\Gamma(\boldsymbol{q})_{s'}) \quad (3)$$

where $\nu^\alpha(\boldsymbol{q})_{s,s'}$ is the coupling group velocity between phonon modes s and s' of wavevector $\boldsymbol{q}$ along the α direction. The total thermal conductivity along α direction κ^α is the sum of κ_p^α and κ_c^α.

The interatomic force constants (IFCs) are extracted using the classical interatomic MYP potential [70] for $MAPbBr_3$ in Large-scale Atomic/Molecular Massively Parallel Simulator (LAMMPS) [71]. Harmonic IFCs are obtained by the finite-difference method [72] with an atomic displacement of 0.005 Å. The third-order IFCs were from Taylor-series fitting by firstly subtracting the contributions of the harmonic IFCs to the interatomic forces. The converged phonon wavevector q-grid size of $10\times10\times8$ was selected for orthorhombic $MAPbBr_3$ and $6\times6\times6$ for tetragonal $MAPbBr_3$, the harmonic and cubic IFCs cutoff were set as 9.5 Å and 5.1 Å for both structures (see the Convergence test in Supplementary Information). Both phonon-isotope scattering and three-phonon scattering were taken into consideration in our study.

Supporting information

The Supporting Information is available free of charge at xx.

The thermal conductivity of $MAPbCl_3$ single crystals, details of FDTR experiment (fitting parameters of FDTR, sensitivity analysis and phase lag measurement, temperature rise correction analysis), structural characterization and analysis of $MAPbBr_3$ single crystals (diffraction peak analysis, whole-pattern fitting refinement analysis, volume fraction analysis, structural evolution induced by steady-state temperature rise in FDTR), theoretical calculation of thermal conductivity (convergence test of parameters, analysis on thermal transport properties of total, population and coherence channel) (PDF).

CRediT authorship contribution statement

Yuting Yu: Data curation, Formal analysis, Investigation, Visualization, Writing – original draft. **Gan Zhang:** Data curation, Formal analysis, Methodology, Writing – original draft. **Zifeng He:** Data curation, Investigation, Visualization, Writing – original draft. **Jing Tu:** Data curation, Formal analysis, Methodology, Validation, Writing – original draft. **Ankit Jain:** Methodology, Software, Validation, Writing – review & editing. **Jonathan A. Malen:** Formal analysis, Methodology, Writing – review & editing. **Derya Baran:** Formal analysis, Writing – review & editing. **Yee Sin Ang:** Formal analysis, Supervision, Writing – review & editing. **Shusheng Xiong:** Funding acquisition, Writing – review & editing. **Dawei Di:** Formal analysis, Resources, Writing – review & editing. **Wee-Liat Ong:** Conceptualization, Formal analysis, Funding acquisition, Methodology, Project administration, Resources, Supervision, Writing – review & editing.

Declaration of competing interest

The authors declare the following financial interests/personal relationships which may be considered as potential competing interests: Wee-Liat Ong reports financial support was provided by National Natural Science Foundation of China. If there are other authors, they declare that they have no known competing financial interests or personal relationships that could have appeared to influence the work reported in this paper.

Acknowledgements

W.-L. Ong was the principal supervisor supported by the National Natural Science Foundation of China [grant number 52576097 and 52350610259], the ZJU-YST Joint Research Center for Fundamental Science, the State Key Laboratory (SKL) of Biobased Transportation Fuel Technology, ZJU-UIUC Institute, and the Zhejiang-Saudi EMC2 Laboratory.

Appendix A. Supplementary data

Supplementary data to this article can be found online at https://doi.org/10.1016/j.mtphys.2026.102107.

Data availability

Data will be made available on request.

References

[1] X. Qian, J. Zhou, G. Chen, Phonon-engineered extreme thermal conductivity materials, Nat. Mater. 20 (2021) 1188–1202, https://doi.org/10.1038/s41563-021-00918-3.
[2] C. Kittel, P. McEuen, Introduction to Solid State Physics, John Wiley & Sons, 2018.
[3] M. Simoncelli, N. Marzari, F. Mauri, Unified theory of thermal transport in crystals and glasses, Nat. Phys. 15 (2019) 809–813, https://doi.org/10.1038/s41567-019-0520-x.
[4] S. Mukhopadhyay, D.S. Parker, B.C. Sales, A.A. Puretzky, M.A. McGuire, L. Lindsay, Two-channel model for ultralow thermal conductivity of crystalline Tl_3VSe_4, Science 360 (2018) 1455–1458, https://doi.org/10.1126/science.aar8072.
[5] Z. Zhang, Y. Guo, M. Bescond, J. Chen, M. Nomura, S. Volz, Heat conduction theory including phonon coherence, Phys. Rev. Lett. 128 (2022): 015901, https://doi.org/10.1103/PhysRevLett.128.015901.
[6] J.-S. Zhou, J.B. Goodenough, Unusual evolution of the magnetic interactions versus structural distortions in RMnO3 perovskites, Phys. Rev. Lett. 96 (2006): 247202, https://doi.org/10.1103/PhysRevLett.96.247202.
[7] S.-Y. Yue, X. Zhang, G. Qin, J. Yang, M. Hu, Insight into the collective vibrational modes driving ultralow thermal conductivity of perovskite solar cells, Phys. Rev. B 94 (2016): 115427, https://doi.org/10.1103/PhysRevB.94.115427.
[8] O. Er-raji, C. Messmer, R.R. Pradhan, O. Fischer, V. Hnapovskyi, S. Kosar, M. Marengo, M. List, J. Faisst, J.P. Jurado, O. Matiash, H.P. Pasanen, A. Prasetio, B. Vishal, S. Zhumagali, A.R. Pininti, Y. Gupta, C. Baretzky, E. Ugur, C. E. Petoukhoff, M. Bivour, E. Aydin, R. Azmi, J. Schön, F. Schindler, M.C. Schubert, U. Schwingenschlögl, F. Laquai, A.A. Said, J. Borchert, P.S.C. Schulze, S. De Wolf, S.W. Glunz, Electron accumulation across the perovskite layer enhances tandem solar cells with textured silicon, Science 390 (2025), https://doi.org/10.1126/science.adx1745.
[9] M. Li, Y. Xie, L. Luo, Z. Zheng, J. Guo, L. He, X. Zheng, R. Liu, Y. Rong, R. Guo, X. Li, B. Dong, In situ impurity phase repair strategy enables highly-efficient perovskite solar cells with periodic photovoltaic performance, Adv. Mater. 37 (2025): 2501057, https://doi.org/10.1002/adma.202501057.
[10] S. Bhattarai, R. Pandey, J. Madan, M.Z. Ansari, M.K. Hossain, M. Amami, S. H. Ahammad, A.N.Z. Rashed, Chlorine-doped perovskite materials for highly efficient perovskite solar cell design offering an efficiency of nearly 29%, Prog. Photovoltaics Res. Appl. 32 (2024) 25–34, https://doi.org/10.1002/pip.3732.
[11] T. Ye, X. Wang, X. Li, A.Q. Yan, S. Ramakrishna, J. Xu, Ultra-high seebeck coefficient and low thermal conductivity of a centimeter-sized perovskite single crystal acquired by a modified fast growth method, J. Mater. Chem. C 5 (2017) 1255–1260, https://doi.org/10.1039/C6TC04594D.
[12] G.A. Elbaz, W.-L. Ong, E.A. Doud, P. Kim, D.W. Paley, X. Roy, J.A. Malen, Phonon speed, not scattering, differentiates thermal transport in lead halide perovskites, Nano Lett. 17 (2017) 5734–5739, https://doi.org/10.1021/acs.nanolett.7b02696.
[13] R. Heiderhoff, T. Haeger, N. Pourdavoud, T. Hu, M. Al-Khafaji, A. Mayer, Y. Chen, H.-C. Scheer, T. Riedl, Thermal conductivity of methylammonium lead halide

perovskite single crystals and thin films: a comparative study, J. Phys. Chem. C 121 (2017) 28306–28311, https://doi.org/10.1021/acs.jpcc.7b11495.
[14] C. Ge, M. Hu, P. Wu, Q. Tan, Z. Chen, Y. Wang, J. Shi, J. Feng, Ultralow thermal conductivity and ultrahigh thermal expansion of single-crystal organic–inorganic hybrid perovskite CH3NH3PbX3 (X = Cl, Br, I), J. Phys. Chem. C 122 (2018) 15973–15978, https://doi.org/10.1021/acs.jpcc.8b05919.
[15] M.E. Manley, K. Hong, P. Yin, S. Chi, Y. Cai, C. Hua, L.L. Daemen, R.P. Hermann, H. Wang, A.F. May, M. Asta, M. Ahmadi, Giant isotope effect on phonon dispersion and thermal conductivity in methylammonium lead iodide, Sci. Adv. 6 (2020), https://doi.org/10.1126/sciadv.aaz1842.
[16] A. Pisoni, J. Jaćimović, O.S. Barišić, M. Spina, R. Gaál, L. Forró, E. Horváth, Ultra-low thermal conductivity in organic–inorganic hybrid perovskite $CH_3NH_3PbI_3$, J. Phys. Chem. Lett. 5 (2014) 2488–2492, https://doi.org/10.1021/jz5012109.
[17] A. Kovalsky, L. Wang, G.T. Marek, C. Burda, J.S. Dyck, Thermal conductivity of CH3NH3PbI3 and CsPbI3: measuring the effect of the methylammonium ion on phonon scattering, J. Phys. Chem. C 121 (2017) 3228–3233, https://doi.org/10.1021/acs.jpcc.6b12231.
[18] R. Mukherjee, Electrical, thermal and elastic properties of methylammonium lead bromide single crystal, Bull. Mater. Sci. 43 (2020) 197, https://doi.org/10.1007/s12034-020-02164-w.
[19] J.-K. Hu, Y.-J. Lee, C.-C. Wu, C.-H. Lee, C.-M. Wu, H.-C. Wu, K. Nawa, K. Kinjo, T. J. Sato, P.-C. Wei, Dual crystal-liquid thermal transport behavior in MAPbCl3, Small 21 (2025): 2408773, https://doi.org/10.1002/smll.202408773.
[20] L. McGovern, M.H. Futscher, L.A. Muscarella, B. Ehrler, Understanding the stability of MAPbBr3 versus MAPbI3: suppression of methylammonium migration and reduction of halide migration, J. Phys. Chem. Lett. 11 (2020) 7127–7132, https://doi.org/10.1021/acs.jpclett.0c01822.
[21] M. Wang, S. Lin, Anisotropic and ultralow phonon thermal transport in organic–inorganic hybrid perovskites: atomistic insights into solar cell thermal management and thermoelectric energy conversion efficiency, Adv. Funct. Mater. 26 (2016) 5297–5306, https://doi.org/10.1002/adfm.201600284.
[22] T. Hata, G. Giorgi, K. Yamashita, The effects of the organic–inorganic interactions on the thermal transport properties of CH3NH3PbI3, Nano Lett. 16 (2016) 2749–2753, https://doi.org/10.1021/acs.nanolett.6b00457.
[23] C. Caddeo, C. Melis, M.I. Saba, A. Filippetti, L. Colombo, A. Mattoni, Tuning the thermal conductivity of methylammonium lead halide by the molecular substructure, Phys. Chem. Chem. Phys. 18 (2016) 24318–24324, https://doi.org/10.1039/C6CP04246E.
[24] T. Zhu, E. Ertekin, Mixed phononic and non-phononic transport in hybrid lead halide perovskites: glass-crystal duality, dynamical disorder, and anharmonicity, Energy Environ. Sci. 12 (2019) 216–229, https://doi.org/10.1039/C8EE02820F.
[25] Y. Gao, W. Ning, X. Zhang, Y. Liu, Y. Zhou, D. Tang, The effective regulation of nanotwinning on the multichannel thermal transport in hybrid organic–inorganic halide perovskite, Nano Energy 82 (2021): 105747, https://doi.org/10.1016/j.nanoen.2021.105747.
[26] J. Yang, A. Jain, W.-L. Ong, Inter-channel conversion between population-/coherence-channel dictates thermal transport in MAPbI3 crystals, Mater. Today Phys. 28 (2022): 100892, https://doi.org/10.1016/j.mtphys.2022.100892.
[27] X. Qian, X. Gu, R. Yang, Lattice thermal conductivity of organic-inorganic hybrid perovskite CH3NH3PbI3, Appl. Phys. Lett. 108 (2016): 063902, https://doi.org/10.1063/1.4941921.
[28] M.A. Haque, S. Kee, D.R. Villalva, W. Ong, D. Baran, Halide perovskites: thermal transport and prospects for thermoelectricity, Adv. Sci. 7 (2020): 1903389, https://doi.org/10.1002/advs.201903389.
[29] Y. Jung, W. Lee, S. Han, B.-S. Kim, S.-J. Yoo, H. Jang, Thermal transport properties of phonons in halide perovskites, Adv. Mater. 35 (2023): 2204872, https://doi.org/10.1002/adma.202204872.
[30] M. Simoncelli, N. Marzari, F. Mauri, Wigner formulation of thermal transport in solids, Phys. Rev. X 12 (2022): 041011, https://doi.org/10.1103/PhysRevX.12.041011.
[31] A. Mattoni, A. Filippetti, M.I. Saba, P. Delugas, Methylammonium rotational dynamics in lead halide perovskite by classical molecular dynamics: the role of temperature, J. Phys. Chem. C 119 (2015) 17421–17428, https://doi.org/10.1021/acs.jpcc.5b04283.
[32] A.N. Beecher, O.E. Semonin, J.M. Skelton, J.M. Frost, M.W. Terban, H. Zhai, A. Alatas, J.S. Owen, A. Walsh, S.J.L. Billinge, Direct observation of dynamic symmetry breaking above room temperature in methylammonium lead iodide perovskite, ACS Energy Lett. 1 (2016) 880–887, https://doi.org/10.1021/acsenergylett.6b00381.
[33] F. Cordero, F. Trequattrini, F. Craciun, A.M. Paoletti, G. Pennesi, G. Zanotti, Cation reorientation and octahedral tilting in the metal-organic perovskites MAPI and FAPI, J. Alloys Compd. 867 (2021): 158210, https://doi.org/10.1016/j.jallcom.2020.158210.
[34] M. Mączka, M. Ptak, Temperature-dependent raman studies of FAPbBr3 and MAPbBr3 perovskites: effect of phase transitions on molecular dynamics and lattice distortion, Solids 3 (2022) 111–121, https://doi.org/10.3390/solids3010008.
[35] A. Poglitsch, D. Weber, Dynamic disorder in methylammoniumtrihalogenoplumbates (II) observed by millimeter-wave spectroscopy, J. Chem. Phys. 87 (1987) 6373–6378, https://doi.org/10.1063/1.453467.
[36] N. Onoda-Yamamuro, T. Matsuo, H. Suga, Calorimetric and IR spectroscopic studies of phase transitions in methylammonium trihalogenoplumbates (II), J. Phys. Chem. Solid. 51 (1990) 1383–1395, https://doi.org/10.1016/0022-3697(90)90021-7.
[37] N. Onoda-Yamamuro, T. Matsuo, H. Suga, Dielectric study of $CH_3NH_3PbX_3$ (X = Cl, Br, I), J. Phys. Chem. Solid. 53 (1992) 935–939, https://doi.org/10.1016/0022-3697(92)90121-S.
[38] N. Onoda-Yamamuro, O. Yamamuro, T. Matsuo, H. Suga, p-T phase relations of CH3NH3PbX3 (X = Cl, Br, I) crystals, J. Phys. Chem. Solid. 53 (1992) 277–281, https://doi.org/10.1016/0022-3697(92)90056-J.
[39] O. Knop, R.E. Wasylishen, M.A. White, T.S. Cameron, M.J.M.V. Oort, Alkylammonium lead halides. Part 2. $CH_3NH_3PbX_3$ (X = Cl, Br, I) perovskites: cuboctahedral halide cages with isotropic cation reorientation, Can. J. Chem. 68 (1990) 412–422, https://doi.org/10.1139/v90-063.
[40] A. Mattoni, A. Filippetti, M.I. Saba, C. Caddeo, P. Delugas, Temperature evolution of methylammonium trihalide vibrations at the atomic scale, J. Phys. Chem. Lett. 7 (2016) 529–535, https://doi.org/10.1021/acs.jpclett.5b02546.
[41] P. Tuo, L. Li, X. Wang, J. Chen, Z. Zhong, B. Xu, F.-Z. Dai, Spontaneous hybrid nano-domain behavior of the organic–inorganic hybrid perovskites, Adv. Funct. Mater. 33 (2023): 2301663, https://doi.org/10.1002/adfm.202301663.
[42] W. Lee, H. Li, A.B. Wong, D. Zhang, M. Lai, Y. Yu, Q. Kong, E. Lin, J.J. Urban, J. C. Grossman, P. Yang, Ultralow thermal conductivity in all-inorganic halide perovskites, Proc. Natl. Acad. Sci. 114 (2017) 8693–8697, https://doi.org/10.1073/pnas.1711744114.
[43] B. Li, Y. Kawakita, Y. Liu, M. Wang, M. Matsuura, K. Shibata, S. Ohira-Kawamura, T. Yamada, S. Lin, K. Nakajima, S. (Frank) Liu, Polar rotor scattering as atomic-level origin of low mobility and thermal conductivity of perovskite CH3NH3PbI3, Nat. Commun. 8 (2017): 16086, https://doi.org/10.1038/ncomms16086.
[44] H. Chen, Z. Yue, D. Ren, H. Zeng, T. Wei, K. Zhao, R. Yang, P. Qiu, L. Chen, X. Shi, Thermal conductivity during phase transitions, Adv. Mater. 31 (2019): 1806518, https://doi.org/10.1002/adma.201806518.
[45] M.T. Agne, P.W. Voorhees, G.J. Snyder, Phase transformation contributions to heat capacity and impact on thermal diffusivity, thermal conductivity, and thermoelectric performance, Adv. Mater. 31 (2019): 1902980, https://doi.org/10.1002/adma.201902980.
[46] K.-H. Wang, L.-C. Li, M. Shellaiah, K. Wen Sun, Structural and photophysical properties of methylammonium lead tribromide (MAPbBr3) single crystals, Sci. Rep. 7 (2017): 13643, https://doi.org/10.1038/s41598-017-13571-1.
[47] F. Ruf, M.F. Aygüler, N. Giesbrecht, B. Rendenbach, A. Magin, P. Docampo, H. Kalt, M. Hetterich, Temperature-dependent studies of exciton binding energy and phase-transition suppression in (Cs,FA,MA)Pb(I,Br)3 perovskites, APL Mater. 7 (2019): 031113, https://doi.org/10.1063/1.5083792.
[48] Y. Yamada, T. Nakamura, M. Endo, A. Wakamiya, Y. Kanemitsu, Near-band-edge optical responses of solution-processed organic–inorganic hybrid perovskite CH3NH3PbI3 on mesoporous TiO2 electrodes, APEX 7 (2014): 032302, https://doi.org/10.7567/APEX.7.032302.
[49] W. Kong, Z. Ye, Z. Qi, B. Zhang, M. Wang, A. Rahimi-Iman, H. Wu, Characterization of an abnormal photoluminescence behavior upon crystal-phase transition of perovskite CH3NH3PbI3, Phys. Chem. Chem. Phys. 17 (2015) 16405–16411, https://doi.org/10.1039/C5CP02605A.
[50] T.S. Kao, Y.-H. Chou, C.-H. Chou, F.-C. Chen, T.-C. Lu, Lasing behaviors upon phase transition in solution-processed perovskite thin films, Appl. Phys. Lett. 105 (2014): 231108, https://doi.org/10.1063/1.4903877.
[51] K. Wu, A. Bera, C. Ma, Y. Du, Y. Yang, L. Li, T. Wu, Temperature-dependent excitonic photoluminescence of hybrid organometal halide perovskite films, Phys. Chem. Chem. Phys. 16 (2014) 22476–22481, https://doi.org/10.1039/C4CP03573A.
[52] V. D'Innocenzo, G. Grancini, M.J.P. Alcocer, A.R.S. Kandada, S.D. Stranks, M. M. Lee, G. Lanzani, H.J. Snaith, A. Petrozza, Excitons versus free charges in organo-lead tri-halide perovskites, Nat. Commun. 5 (2014) 3586, https://doi.org/10.1038/ncomms4586.
[53] A. Osherov, E.M. Hutter, K. Galkowski, R. Brenes, D.K. Maude, R.J. Nicholas, P. Plochocka, V. Bulović, T.J. Savenije, S.D. Stranks, The impact of phase retention on the structural and optoelectronic properties of metal halide perovskites, Adv. Mater. 28 (2016) 10757–10763, https://doi.org/10.1002/adma.201604019.
[54] K. Schötz, A.M. Askar, A. Köhler, K. Shankar, F. Panzer, Investigating the tetragonal-To-orthorhombic phase transition of methylammonium lead iodide single crystals by detailed photoluminescence analysis, Adv. Opt. Mater. 8 (2020): 2000455, https://doi.org/10.1002/adom.202000455.
[55] C. Wehrenfennig, M. Liu, H.J. Snaith, M.B. Johnston, L.M. Herz, Charge carrier recombination channels in the low-temperature phase of organic-inorganic lead halide perovskite thin films, APL Mater. 2 (2014): 081513, https://doi.org/10.1063/1.4891595.
[56] B. Yang, W. Ming, M.-H. Du, J.K. Keum, A.A. Puretzky, C.M. Rouleau, J. Huang, D. B. Geohegan, X. Wang, K. Xiao, Real-time observation of order-disorder transformation of organic cations induced phase transition and anomalous photoluminescence in hybrid perovskites, Adv. Mater. 30 (2018): 1705801, https://doi.org/10.1002/adma.201705801.
[57] P.S. Whitfield, N. Herron, W.E. Guise, K. Page, Y.Q. Cheng, I. Milas, M.K. Crawford, Structures, phase transitions and tricritical behavior of the hybrid perovskite methyl ammonium lead iodide, Sci. Rep. 6 (2016): 35685, https://doi.org/10.1038/srep35685.
[58] P. Jiang, H. Ban, Transient and steady-state temperature rise in three-dimensional anisotropic layered structures in pump-probe thermoreflectance experiments, J. Phys. Appl. Phys. 54 (2020): 035304, https://doi.org/10.1088/1361-6463/abbd64.
[59] Y. Ahn, J. Zhang, Z. Chu, D.A. Walko, S.O. Hruszkewycz, E.E. Fullerton, P.G. Evans, H. Wen, Ultrafast switching of interfacial thermal conductance, ACS Nano 17 (2023) 18843–18849, https://doi.org/10.1021/acsnano.3c03628.

[60] C.-W. Nan, Physics of inhomogeneous inorganic materials, Prog. Mater. Sci. 37 (1993) 1–116, https://doi.org/10.1016/0079-6425(93)90004-5.
[61] N. Sarikhani, Z.S. Arabshahi, A.A. Saberi, A.Z. Moshfegh, Unified modeling and experimental realization of electrical and thermal percolation in polymer composites, Appl. Phys. Rev. 9 (2022): 041403, https://doi.org/10.1063/5.0089445.
[62] K.J. Lee, B. Turedi, A. Giugni, M.N. Lintangpradipto, A.A. Zhumekenov, A. Y. Alsalloum, J.-H. Min, I. Dursun, R. Naphade, S. Mitra, I.S. Roqan, B.S. Ooi, O. F. Mohammed, E.D. Fabrizio, N. Cho, O.M. Bakr, Domain-size-dependent residual stress governs the phase-transition and photoluminescence behavior of methylammonium lead iodide, Adv. Funct. Mater. 31 (2021): 2008088, https://doi.org/10.1002/adfm.202008088.
[63] J. Wu, J. Chen, H. Wang, Phase transition kinetics of MAPbI3 for tetragonal-to-orthorhombic evolution, JACS Au 3 (2023) 1205–1212, https://doi.org/10.1021/jacsau.3c00060.
[64] D. Shi, V. Adinolfi, R. Comin, M. Yuan, E. Alarousu, A. Buin, Y. Chen, S. Hoogland, A. Rothenberger, K. Katsiev, Y. Losovyj, X. Zhang, P.A. Dowben, O.F. Mohammed, E.H. Sargent, O.M. Bakr, Low trap-state density and long carrier diffusion in organolead trihalide perovskite single crystals, Science 347 (2015) 519–522, https://doi.org/10.1126/science.aaa2725.
[65] A.J. Schmidt, R. Cheaito, M. Chiesa, A frequency-domain thermoreflectance method for the characterization of thermal properties, Rev. Sci. Instrum. 80 (2009): 094901, https://doi.org/10.1063/1.3212673.
[66] D.G. Cahill, Analysis of heat flow in layered structures for time-domain thermoreflectance, Rev. Sci. Instrum. 75 (2004) 5119–5122, https://doi.org/10.1063/1.1819431.
[67] A.J. Schmidt, X. Chen, G. Chen, Pulse accumulation, radial heat conduction, and anisotropic thermal conductivity in pump-probe transient thermoreflectance, Rev. Sci. Instrum. 79 (2008): 114902, https://doi.org/10.1063/1.3006335.
[68] J. Tu, M.A. Haque, D. Baran, W.-L. Ong, Logarithmic sensitivity ratio elucidates thermal transport physics in multivariate thermoreflectance experiments, Fundam. Res. 5 (2025) 288–295, https://doi.org/10.1016/j.fmre.2023.01.010.
[69] J. Tu, W.-L. Ong, A universal sensitivity matrix reduction technique (SMART) to uncover governing thermal transport relationships, Int. J. Heat Mass Tran. 206 (2023): 123949, https://doi.org/10.1016/j.ijheatmasstransfer.2023.123949.
[70] T. Hata, G. Giorgi, K. Yamashita, C. Caddeo, A. Mattoni, Development of a classical interatomic potential for $MAPbBr_3$, J. Phys. Chem. C 121 (2017) 3724–3733, https://doi.org/10.1021/acs.jpcc.6b11298.
[71] S. Plimpton, Fast parallel algorithms for short-range molecular dynamics, J. Comput. Phys. 117 (1995) 1–19, https://doi.org/10.1006/jcph.1995.1039.
[72] A.J.H. McGaughey, A. Jain, H.-Y. Kim, Phonon properties and thermal conductivity from first principles, lattice dynamics, and the boltzmann transport equation, J. Appl. Phys. 125 (2019): 011101, https://doi.org/10.1063/1.5064602.